Nuclear Engineering and Design 454 (2026) 114942

Contents lists available at ScienceDirect

Nuclear Engineering and Design

journal homepage: www.elsevier.com/locate/nucengdes

CFD simulations of hydrodynamics and aerosol pool scrubbing tests under low momentum injection

A. Dehbi [a,*], N. Ghendour [b], B. Niceno [a], D. Suckow [b], M. Klauck [c]

[a] Center for Scientific Computing, Theory and Data, Paul Scherrer Institut, Villigen, Switzerland
[b] Center for Reactor Physics and Thermal-Hydraulics, Paul Scherrer Institut, Villigen, Switzerland
[c] Forschungszentrum Jülich GmbH, Institute for Energy and Climate Research, Jülich, Germany

ARTICLE INFO

Keywords:
CFD
Two-phase flow
Aerosol pool scrubbing
VOF
Lagrangian particle tracking

ABSTRACT

One way to mitigate the consequences of fission product releases in nuclear plants is to direct the contaminated carrier gas through water pools where a large fraction of the particles may be scrubbed. Current models predicting the particle removal rates in pools are mostly one dimensional in nature and rely on empirical correlations and over-simplifications. On the other hand, Computational Fluid Dynamics (CFD) has recently become a mature tool to simulate low momentum two-phase flows and can thus be used provided the underlying models are properly validated. The HECTAR project, which is a joint effort between the Paul Scherrer Institute (PSI) and the Research Center Jülich (FZJ), aims to provide detailed and high-resolution experimental data to support CFD hydrodynamics and particle removal models.

In this paper, we present CFD validation results for selected tests in HECTAR. Firstly, hydrodynamics CFD simulations are conducted using the ANSYS Fluent commercial code. The Volume of Fluid (VOF) method is used to track the interface as the bubble rises in the pool. In a second step, particles with different sizes are followed using the Euler/Lagrange methodology. Removal of particles from the bubble is complex, owing to the break-up and coalescence phenomena, and a full description of the physics is yet to be developed. Nevertheless, the problem is simplified by looking at the injector region where the velocities inside the globule are largest, and hence particle retention there is the greatest.

Results show that CFD can capture reasonably well the main measures of bubble hydrodynamics (void profile, globule detachment frequency, globule size, etc.). Likewise, simulations provide good estimates of the particle retention rates in the injection region. Detailed CFD information on the flow field shed light on why particle removal is globally insensitive to gas injection flow rates for the ranges under consideration.

1. Introduction

Following a nuclear severe accident, the degraded cores produce fission product (FP) aerosols that can reach the environment if not retained by either natural forces or dedicated filtering systems. Before being potentially released to the environment, FP typically move through water pools where they may be removed to a certain extent.In BWRs the wetwell pool can serve for this purpose (Dallman et al., 1990), whereas in PWRs the quench tanks or the steam generator secondary side pool (Lind et al., 2011) can act as scrubbing medium for the FP. In addition, in the aftermath of the Fukushima accident, plants around the world have backfitted their units with so-called filtered containment venting systems (FCVSs) (Albiol et al., 2018), with the aim of greatly reducing a hypothetical FP source term through pool scrubbing action during containment depressurization.

Due to its high safety relevance, FP pool scrubbing has been studied by numerous research teams ever since the 1980s, both experimentally and analytically.

In analytical studies, 1D codes have been developed with simplified models for aerosol removal by pools.The most widely codes include SUPRA (Wassel et al., 1985), SPARC (Owczarski and Burk, 1991) and BUSCA (Ramsdale and Güntay, 1995). Some of these codes have been integrated into severe accident system codes such as MELCOR (Gauntt et al., 2000) or COCOSYS (Arndt et al., 2019).However, the pool scrubbing models used in 1D codes rely mostly on empirical correlations deduced from simplified hydrodynamics and aerosol experiments performed at various organizations, e.g. (Paul et al., 1985; Paul et al., 1991;

* Corresponding author.
E-mail address: abdel.dehbi@psi.ch (A. Dehbi).

https://doi.org/10.1016/j.nucengdes.2026.114942
Received 27 January 2026; Received in revised form 19 March 2026; Accepted 12 April 2026
Available online 15 April 2026

Nomenclature

CFD	Computational Fluid Dynamics
CFL	Courant-Friedrichs-Lew number
C_D	Particle drag coefficient
DF	Decontamination Factor
D_{inj}	Injector diameter
d_p	Particle diameter
FCVS	Filtered Containment Venting System
FP	Fission Products
FZJ	Forschungs-Zentrum Jülich GmbH
F_{st}	Surface tension force
g	Gravity acceleration vector
k	Local interface curvature
HECTAR	Hydrodynamic Experiments to Characterize Aerosol Retention
HSC	High-Speed Camera
IPRESCA	Integration of Pool scrubbing Research to Enhance Source-term Calculations
IT	Interface Tracking
LPM	Liter Per Minute
LPT	Lagrangian Particle Tracking
LS	Level Set
n	Normal unit vector
NITA	Non-Iterative Time Advancement
p	Pressure
PASSAM	Passive and Active Systems on Severe Accident source term Mitigation
PSI	Paul Scherrer Institut
Re_p	Particle Reynolds number
SAAB	Severe Accident Aerosol Behavior facility
t	Time
TRISTAN	Tube Rupture In Steam generaTor multi-phAse flow investigatioNs
TSO	Technical Support Organizations
U	Gas velocity
U_p	Particle velocity
VOF	Volume of Fluid
WMS	Wire Mesh Sensor
x	coordinate

Subscript

g	Gas
p	Particle
w	Water

Greek

α	Volume fraction
β_i	Constants
ρ	Mixture density
ρ_p	Particle density
ρ_l	Liquid density
ρ_g	Gas density
μ	Mixture molecular viscosity
μ_g	Gas molecular viscosity
μ_l	Liquid molecular viscosity
σ	Surface tension
ν_g	Gas kinematic viscosity

Marcos-Crespo et al., 1993). As such, models based on these experiments typically fail to describe the pool scrubbing phenomena when applied in realistic conditions (Herranz et al., 2020). Large discrepancies are noted, with mostly underestimation of the particle removal rates, pointing to the fact that important scrubbing phenomena are missing from the simplistic 1D treatments of the underlying physics.

As mentioned in (Gupta et al., 2023), the lack of systematic experimental databases limits the generality of the 1D models and reduces confidence in their application across a wide range of realistic accident scenarios. To help establish the state-of-the-art in pool scrubbing and pinpoint areas where uncertainties are highest, the IPRESCA (Integration of Pool scrubbing Research to Enhance Source-term Calculations) project has been set-up. The project aimed to promote international integration of pool scrubbing research by granting support to experimental and analytical research and offering a novel platform to exchange information as well as conduct comparative validation benchmarks with e.g. lumped parameter (LP) (Marchetto et al., 2022) or computational fluid dynamics (CFD) tools (Dehbi et al., 2022). The project features the participation of more than 30 organizations, including research institutes, technical support organizations (TSOs) and universities.

Similarly, the PASSAM (Passive and Active Systems on Severe Accident source term Mitigation) (Albiol et al., 2018) was an R&D project focused on experimental investigations with the aim of helping to mitigate severe accidents in a Nuclear Power Plant (NPP). The project looked specifically at pool scrubbing at conditions that are as realistic as feasible. The aim is to develop improved models based on the collected data and eventually enhance understanding of severe accident management measures and guidelines.

In contrast with LP code modeling, 3D treatments of the pool scrubbing phenomena with CFD reduce much of the empiricism and offer in principle the preferred framework for examining aerosol removal mechanisms in detail and for developing improved models suitable for implementation in 1D codes. However, multiphase CFD is a new tool that requires substantial validation before being used with confidence. In recent times, CFD has been applied to pool scrubbing hydrodynamics under low momentum situations.To validate codes, recent experiments have proposed more refined measurements and presented so-called CFD-grade data that are specifically designed to validate 3D CFD codes.

With the aim of clarifying the two-phase flow in pool scrubbing, Abe et al. (Abe et al., 2018) used a high-speed video camera to quantify the bubble size and aspect ratio. In addition, the researchers measured void-fraction profiles and bubble velocity using a wire-mesh sensor (WMS) for a range of flow rates and water submergence heights. The authors concluded that significant differences existed between the acquired data and models implemented in the MELCOR code. For example, the bubble aspect-ratio was more flattened and displayed a wider distribution than the MELCOR model. The gas velocity just above the injector nozzle was also larger than the swarm velocity computed with MELCOR. Only in the far field was the rise velocity similar to that predicted by MELCOR.

Nakamura et al. (Nakamura et al., 2019) used a similar WMS instrument and a high-speed camera (HSC) to characterize bubble motion for a range of injection gas flow rate, steam fractions, subcooling temperature and water submergence.

Fujiwara et al. (Fujiwara et al., 2019) concentrated on a single oil droplet – which is a proxy for an air bubble- to investigate the internal velocity field and permitted a direct comparison between the interface velocity and the one predicted by the model in the MELCOR code.

Within IPRESCA (Gupta et al., 2023), a CFD hydrodynamics benchmark was proposed based on a simple hypothetical geometry (Dehbi et al., 2022). Reasonable agreement was found between interface (IT) tracking simulations near the injector, but discrepancies increase as one moves toward the free surface. The disagreement between the Euler-Euler two-fluid and IT results was found to be substantial throughout the domain.

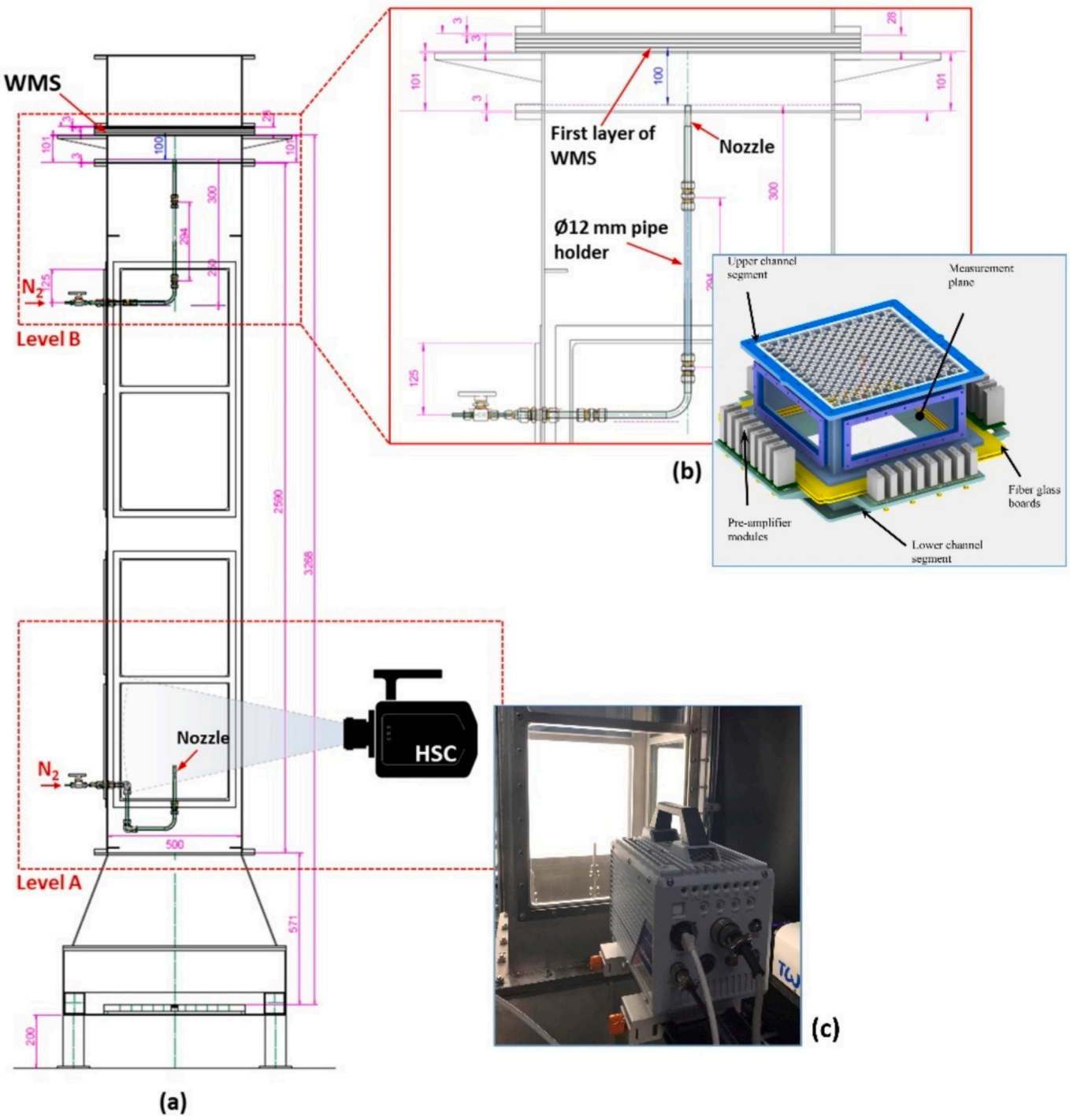

Fig. 1. Overview of the TRISTAN hydrodynamic facility (Ghendour et al., 2026) (a) Test section; (b) Wire mesh sensor; (c) High speed camera

Liao et al. (Liao et al., 2022) used the CFD VOF approach to simulate with OpenFOAM the room temperature hydrodynamics tests of Abe et al. (Abe et al., 2018) at flow rates of 8.5–84.8 LPM so that the Weber number (defined as $\rho_w U^2 D_{inj}/\sigma$) is of the order of 2.5×10^4–2.5×10^5. The simulation spanned thus both the high velocity globule regime as well as the jet regime ($We > 10^5$). The pool consists of a square cross section of width 0.5 m and submergence 1.1 m, while the gas is injected through a 6 mm ID orifice. The code was able to predict time-averaged void profiles as well as rise velocity of individual bubbles.

In contrast to bubble hydrodynamics simulations, CFD investigations of particle motion inside the bubble are quite rare.One of the first such investigations is due to Laker et al. (Laker and Ghiaasiaan, 2004) who determined aerosol particles removal considering particle trajectories inside the rising bubble. A similar work was performed by Motegi et al. (Motegi et al., 2022). These studies however assign a constant spherical shape to the bubble and assume an internal flow field based on the Hills vortex. As such, the bubble deformation, coalescence and break-up are not addressed, and thus the models are not fully predictive.

Kunšek et al. (Kunšek et al., 2022) proposed a theoretical Euler-Euler CFD model for solid particles transport inside a rising spherical bubble. While overly simplified, this work is one of the first to use local instantaneous gas velocity scales to infer particle removal from the gas field. Agreement between the predictions and two sets of experimental data was deemed satisfactory.

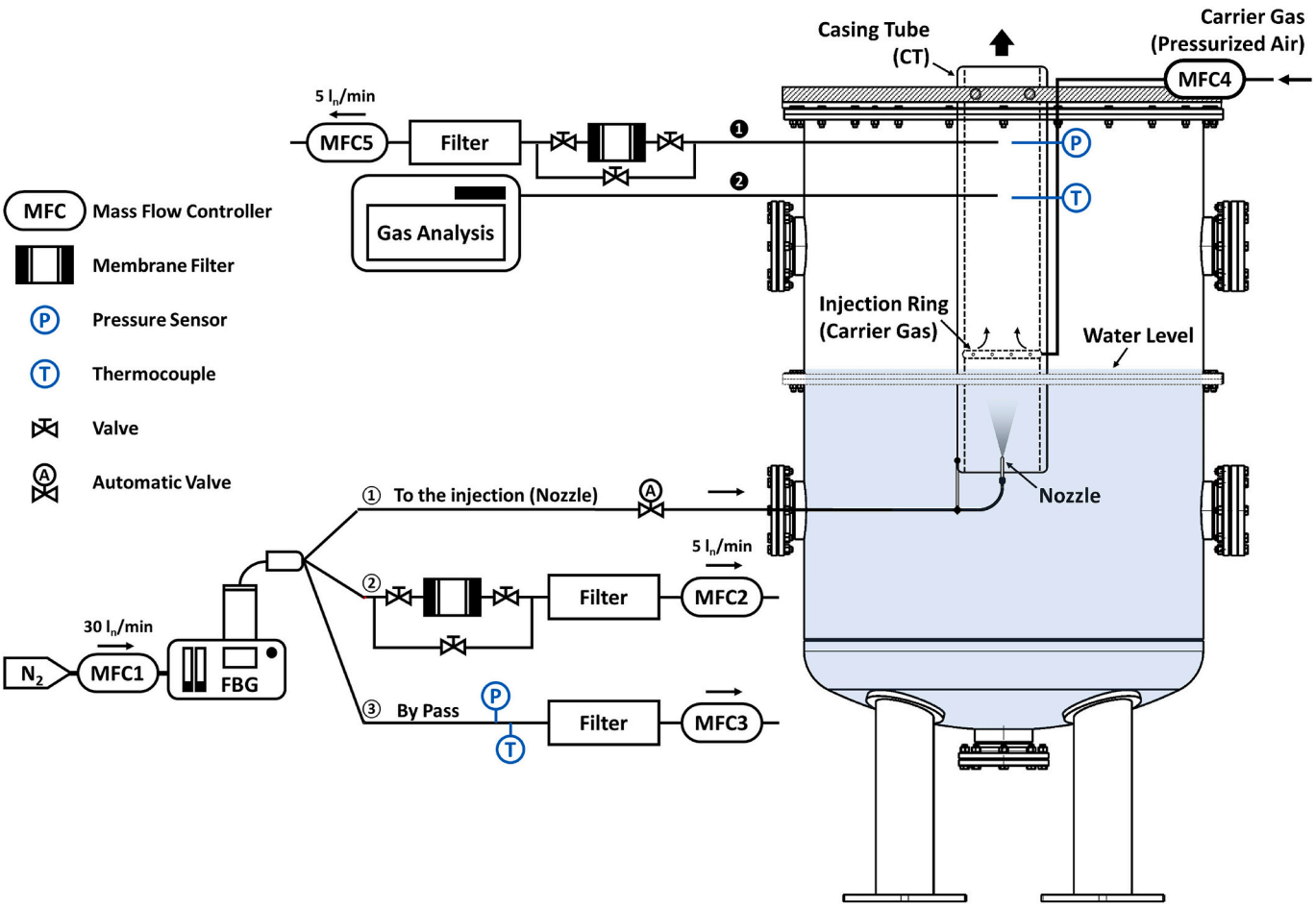

Fig. 2. Aerosol test section within the SAAB facility (Ghendour et al., 2026)

Recently, Sun used the Euler-Lagrange approach to simulate particle removal by a fixed-size spherical (Sun, 2021) and ellipsoidal (Sun, 2022) bubble rising in a pool. The study introduced significant simplifications, that is, the bubble shape, rise velocity, and internal circulation inside the bubble were prescribed. As a result, the model is not fully predictive and is useful only for tiny bubbles of the order of 1–2 mm. This range is well below the typical bubble sizes in nuclear applications (5 mm–30 mm).

Zhu et al. (Zhu et al., 2019) were one of the first investigators to use the IT approach combined with Lagrangian Particle Tracking (LPT) to determine the trajectories and removal of solid particles entrained within a rising bubble. The latter was allowed to naturally deform as it rose in the pool. The injection flow rate and generated bubble were small so that no break-up or coalescence took place. A quantitative correlation of particle deposition fraction versus Stokes number was proposed, but no validation of the methodology was presented as the problem set-up was hypothetical.

In the present investigation, the objective is to validate the CFD methodology for aerosol pool scrubbing under low momentum gas injection. Simulations of the hydrodynamics field are performed with the VOF approach, while particle transport is performed within the Euler-Lagrange formulation. The validation database stems from recent CFD-grade experiments conducted within the HECTAR project (Ghendour et al., 2026) described next.

2. The Hectar pool scrubbing project

The primary aim of the HECTAR (Hydrodynamic Experiments to Characterize Aerosol Retention) project (Ghendour et al., 2026) is to provide detailed experimental data to enhance hydrodynamics and particle removal models used in pool scrubbing codes. The focus is on two-phase hydrodynamics and particle removal near the injector region, where most of the aerosol mass is typically removed. To meet this objective, a series of hydrodynamics and aerosol retention experiments were carried out in two complementary facilities: TRISTAN (PSI) and SAAB (FZJ). Both facilities were operated under identical test conditions (geometry, flow regime, and operating parameters), enabling a direct link between the hydrodynamics data from TRISTAN and the aerosol retention results from SAAB.

A brief overview of the HECTAR experimental facilities is provided below. The full facility descriptions are given in the experimental work done within the HECTAR project framework (Ghendour et al., 2026).

2.1. The Hectar hydrodynamics tests in TRISTAN

The hydrodynamic experiments are carried out in the TRISTAN test facility at the Paul Scherrer Institute. The TRISTAN facility, depicted in Fig. 1, is a tank with a square cross-section with 500 mm side length and an overall height that can reach 6100 mm. The water level inside the facility is set to 300 mm above the injector. Gas is injected through a submerged nozzle with different inner diameters. Data are collected on the bubble and pool hydrodynamics using advanced instrumentation to provide detailed, high-quality data on the gas-liquid flow fields.

The bubble size distribution, interfacial area, interfacial area concentration, Gas Void Fraction (GVF), and bubble velocity are derived from the Wire Mesh Sensor (WMS) signals. A sophisticated bubble reconstruction algorithm calculates the three-dimensional bubble shape and bubble volume. HSC recordings provide globule detachment frequency from the injector and the globule/bubble location as a function

of time. In addition, redundant data on the bubble size, shape, and velocity are deduced from image analysis of the HSC data to compare with the WMS data.

2.2. The HECTAR aerosol pool scrubbing tests in SAAB

The aerosol pool scrubbing experiments are conducted at the SAAB facility (FZJ/Germany). Particular emphasis was to design experiments which ensure identical conditions as for the bubble hydrodynamic tests performed in TRISTAN. The results characterize the relationships between hydrodynamics and retention performance for the investigated aerosol particles.

SAAB is a large-scale stainless steel cylindrical test facility with an inner diameter of 1.5 m and a total height of up to 8 m. The facility operates at ambient pressure. SAAB is specifically designed for high-quality, well-controlled aerosol experiments which differ significantly from the low-flow conditions of the HECTAR project experiments. Accordingly, modifications were made to the injection and sampling systems. The aerosol test section within SAAB is shown schematically in Fig. 2. The membrane filter measure particle mass concentration at the inlet and outlet, from which the Decontamination Factor (DF) is determined. Since interest in this research is in the injection zone, only a short section of the SAAB facility was used. The aerosol-laden flow is injected into the pool with submergence 30 cm above the injector. A casing tube was used to channel the flow upwards, and an additional gas flow was supplied above the water level to ensure that particles leaving the water surface do no settle back into the pool due to the small upstream carrier gas flow.

3. Modeling the two-phase flow

3.1. Liquid-gas modeling with the Volume of Fluid (VOF) method

Pool scrubbing hydrodynamics involves many intermingled phenomena, namely globule formation at the injector, subsequent bubble break-up and coalescence, bubble shrinkage due to condensation, etc. To capture these phenomena in a rigorous manner, gas-liquid interface tracking is essential. There are many IT methods that have been proposed.The most widely used methods are the Level Set [LS] (Sussman, 1994) and Volume of Fluid (VOF) (Hirt and Nichols, 1981).

The LS is known to capture the interface shape quite accurately and is particularly suited for free surface flows. However, it does not conserve mass, which makes it unattractive for pool scrubbing applications. On the other hand, the Volume of Fluid (VOF) method is the standard model used by many investigators and implemented in CFD codes such as ANSYS Fluent (ANSYS, Inc., 2022) or OpenFOAM (Liao et al., 2022). With its inherent mass conservation feature, the VOF method provides reliable predictions of the main two-phase phenomena. The two-phase flow consists of two incompressible, isothermal, and immiscible fluids, and is treated as a mixture with a single set of conservation equations. To track the interface, the gas volume fraction is defined as 0 in cells containing only the liquid, and 1 in cells containing only the gas. In interface cells having both liquid and gas content, the volume fraction α_g of the gas is computed using a transport equation as follows:

$$\frac{\partial \alpha_g}{\partial t} + \nabla\cdot(\alpha_g U) = 0 \tag{1}$$

The density and viscosity in interface cells are weighted by the volume fraction as follows:

$$\rho = \alpha_g \rho_g + (1-\alpha_g)\rho_l \tag{2}$$

$$\mu = \alpha_g \mu_g + (1-\alpha_g)\mu_l \tag{3}$$

The velocity field of the mixture obeys the continuity and incompressible form of the Navier-Stokes conservation equations, that is:

$$\nabla\cdot U = 0 \tag{4}$$

$$\frac{\partial(\rho U)}{\partial t} + \nabla\cdot(UU) = -\nabla p + \rho g + \nabla\cdot\mu\left(\nabla U + \nabla U^T\right) + F_{st} \tag{5}$$

The surface tension force F_{st} acting at the interface is modeled following the Continuum Surface Force (CSF) model proposed by prescription by Brackbill et al. (Brackbill et al., 1992):

$$F_{st} = \sigma k \mathbf{n} \tag{6}$$

Above σ is the surface tension, k the local interface curvature and **n** the unit vector normal to the interface. This model has been shown to provide reasonable descriptions of bubble growth and detachment from orifice injectors. In similar fashion to previous studies (Liao et al., 2022) no turbulence models are used. This is a reasonable approach as we are dealing with low momentum flows within a stagnant pool. Therefore, the numerical mesh will resolve the small-scale velocity fluctuations.

3.2. Lagrangian Particle Tracking (LPT) and Coupling with the VOF computation

The motion of particles inside the gas globule/bubbles is modeled using the Lagrangian approach. We consider a rigid point-wise particle which is entrained in the gas flow at isothermal conditions. The only forces acting on the particle are taken to be drag and gravity. Brownian diffusion is ignored as particles in this study have diameters greater than 0.5 μm. The lift force is also neglected. The vector force balance on a spherical particle inside the bubble reduces then to:

$$\frac{dU_p}{dt} = \frac{18\mu_g}{\varrho_p d_p^2} C_D \frac{Re_p}{24}(U - U_p) + g \tag{7}$$

where U is the fluid velocity vector, U_p the particle velocity vector, ρ_p the particle density, d_p the particle geometric diameter, μ_g the gas molecular viscosity, g the gravity acceleration vector, C_D the drag coefficient and Re_p the particle Reynolds number defined as:

$$Re_p = \frac{d_p|U - U_p|}{\nu_g} \tag{8}$$

Above ν_g is the gas kinematic viscosity. The drag coefficient C_D is computed in the ANSYS Fluent code (ANSYS, Inc., 2022) from the following equation:

$$C_D = \beta_1 + \frac{\beta_2}{Re_p} + \frac{\beta_3}{Re_p^2} \tag{9}$$

where the β's are constants which apply to spherical particles for wide ranges of Re_p.

Since a particle typically does not coincide with the cell nodes, interpolation by the code is used to estimate the gas velocity at particle location. Eq. (6) is supplemented by the definition of particle velocity in order to compute the particle trajectory:

$$U_p = \frac{d\mathbf{x}}{dt} \tag{10}$$

The VOF-LPT coupling is conducted as follows: at each VOF fluid time step, the particle equations of motion are solved based on the frozen flow field. Particles are thus advanced in time to their new location using smaller integration sub-time steps to guarantee computation accuracy of the trajectories. The code uses an algorithm to gradually decrease the particle time step until the next predicted location of the particle no longer changes. This procedure is carried out until the particle location at the end of the fluid time step is reached.

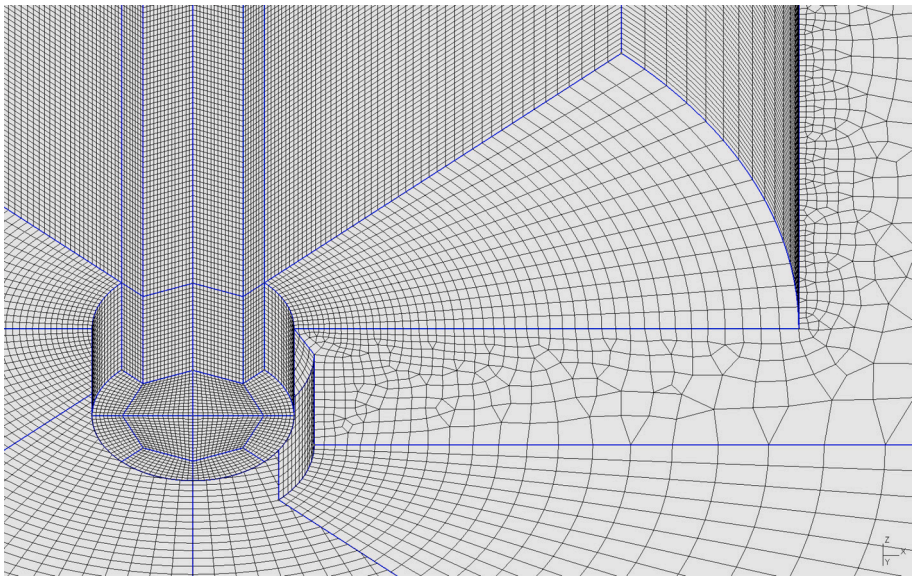

Fig. 3. Detail of the computational mesh in the vicinity of the nozzle, viewed from below. The figure highlights the structured sector-based refinement around the injector and its transition toward the coarser outer-domain blocks. Some blocks are hidden for better visibility.

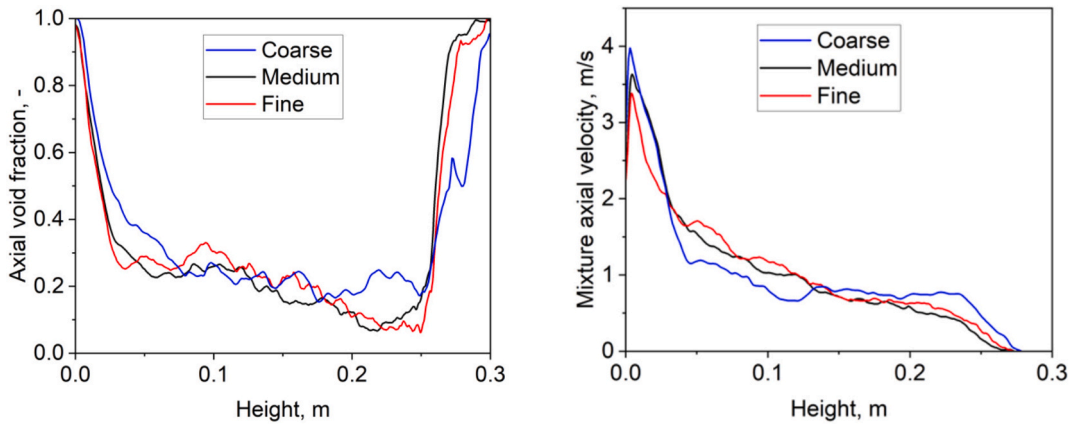

Fig. 4. Mesh independency study. Left: Mean void fraction; Right: Mean mixture velocity magnitude.

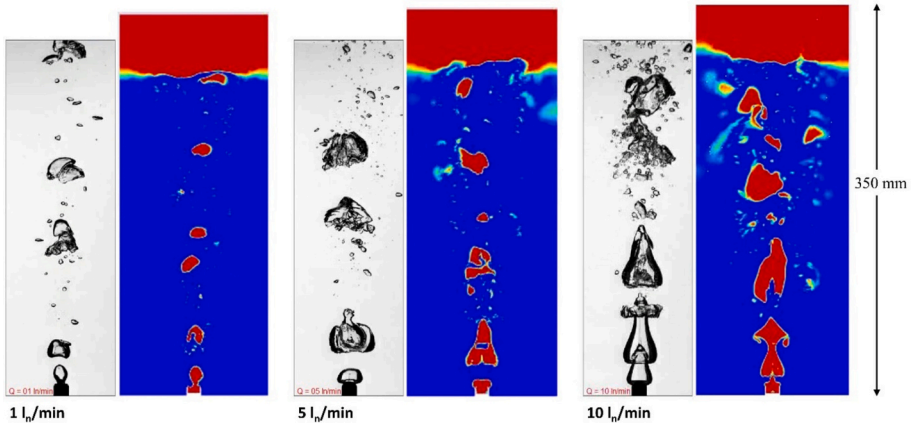

Fig. 5. Instantaneous realizatons of flow patterns for different flow rates (black and white: HSC snaphots; in color: CFD).

3.3. Numerical Grid and Grid-independence tests

The computational grid was generated in Gmsh using a hybrid multi-block strategy. Above the nozzle opening, two characteristic groups of volumes were defined: four structured "core" blocks, surrounded by eight structured "ring" blocks. The mesh spacing in this region was selected such that the nozzle opening diameter was resolved by approximately 44 cells. The four core blocks, together with the

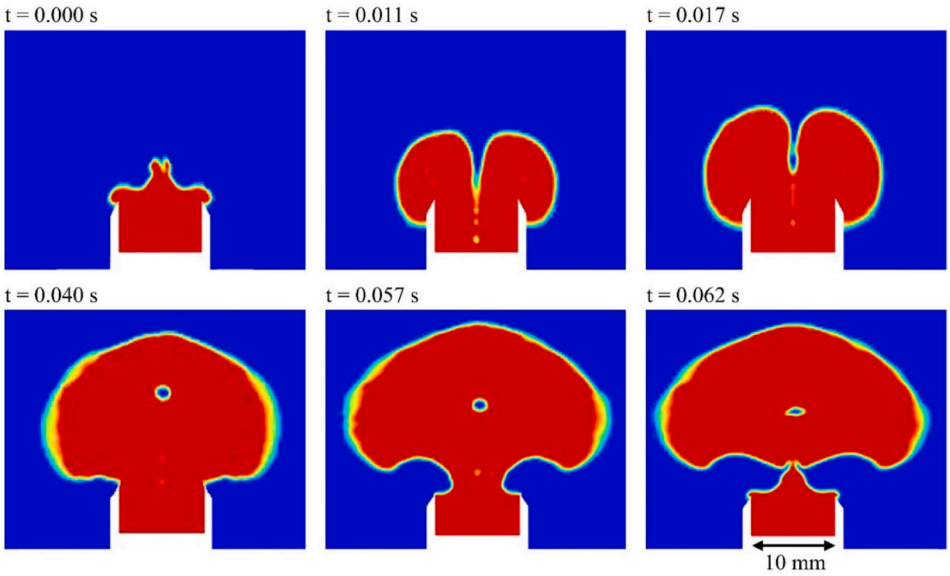

Fig. 6. A typical realization of globule detachment from the injector. 10 LPM case (Time progression: from left to right and from top to bottom).

Table 1
Globule detachment frequency.

Injection flow rate LPM	Test data Globule #/s	CFD prediction Globule #/s
1	16	20
3	19	22
5	21	22
10	22	22

surrounding ring blocks, are shown in Fig. 3; two of the ring blocks were hidden in the figure for better visibility. The axial resolution in this region was chosen so that the axial grid spacing was as close as possible to the radial and tangential grid spacing. In total, 900 cell rows were used in the axial direction. The inner ring blocks are further surrounded by eight additional blocks that cover the region near the axis, where the strongest bubble dynamics are expected. Six of these blocks are also visible in Fig. 3. The outermost region, located close to the vessel walls and farther away from the central high-dynamics region, was meshed with blocks that are not purely hexahedral, but hexadominated. One such block is also shown in Fig. 3. The Gmsh script to create this grid is available from the authors upon request.

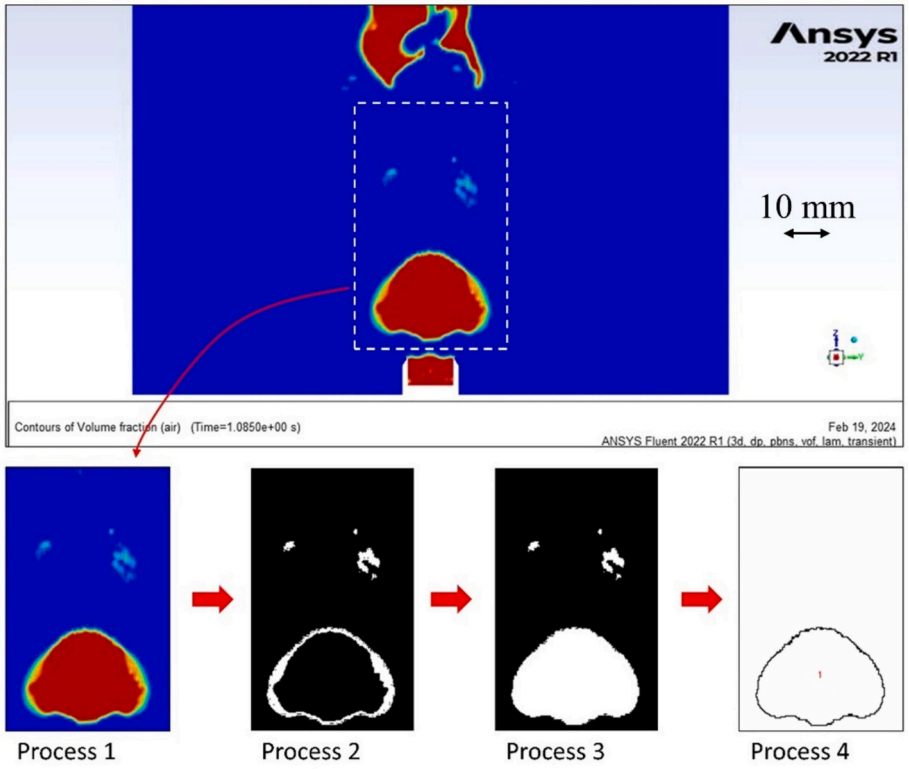

Fig. 7. Image processing of the CFD void snapshots.

Table 2
Globule diameter at detachment time.

Injection flow rate LPM	CFD prediction central plane, 0° mean diameter mm	CFD prediction central plane 90° mean diameter mm	CFD prediction average mean diameter mm	Test data mean diameter mm
1	12.1 ± 0.68	12.1 ± 1.0	12.1	15.2 ± 3.5
3	19.8 ± 3.1	19.7 ± 2.9	19.8	21.6 ± 4.5
5	25.9 ± 3.8	24.6 ± 3.9	25.2	24.9 ± 4.6
10	30.2 ± 3.5	30.6 ± 3.3	30.4	32.0 ± 5.4

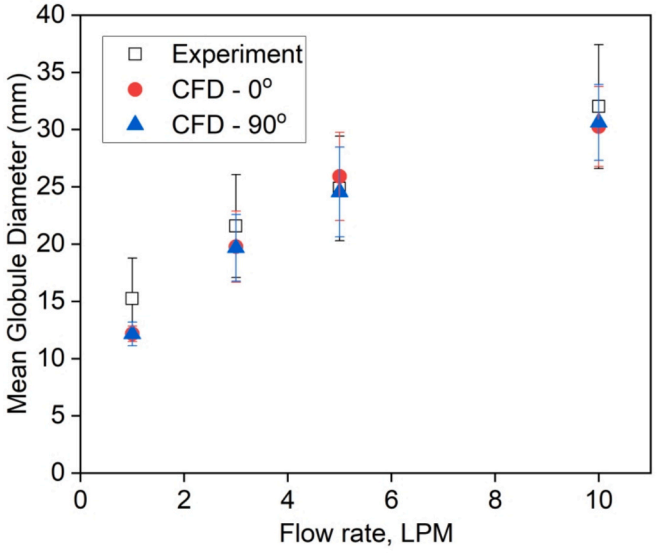

Fig. 8. Effective globule diameter: CFD vs experimental data.

Coarse, medium and fine meshes were produced, with a number of nodes being respectively 0.79 million, 2.2 million and 7.1 million. The selected conditions for this mesh-independence test are as follows:

Nozzle diameter: 10 mm; injection flow rate: 10 LPM; water submergence above nozzle: 0.3 m.

The time-averaged void fraction and mixture velocity along the vertical axis for the 10 LPM case are shown in Fig. 4 for different mesh resolutions.It can be seen that the medium and fine grids provide similar predictions, while the coarse mesh depicts some deviations. Hence we conclude that the medium mesh provides adequate resolution for the simulations. This mesh is thus adopted for the production computations performed.

3.4. Numerical settings

The numerical settings are chosen to reflect both accuracy and robustness in the simulations. The PISO scheme is used for pressure-velocity coupling, while second order upwind scheme is employed for the momentum equation. To help improved the convergence of the VOF calculation, the "modified body force weighted" method is used for the pressure interpolation scheme. Furthermore, the Geo-Reconstruct method computes the locus of the interface using piecewise-linear schemes. This is the most accurate approach available in the code. The transient integration is first order in time, and the VOF Eq. (1) is discretized explicitly, which leads to restriction of the CFL to less than 1. In practice, an adaptive time-step was used, corresponding to a maximum CFL of 0.8. This has helped keep stable simulations for all the runs.The Non-Iterative Time Advancement (NITA) method was used to treat the transient, leading to substantial CPU savings compared to the iterative counterpart.

3.5. Geometric and boundary conditions

Due to high CPU costs, simulations are limited to a sub-set of the experimental HECTAR test matrix. The CFD analyses covered gas injection flow rates of 1, 3, 5 and 10 LPM. The inner diameter of the injector was 10 mm and the water submergence was 0.3 m above the injector. At the injector, an inlet mass flow rate was assigned, whereas atmospheric pressure was set for the outlet surface which is open to the ambient. Reversed flow from the latter is allowed and consists entirely of air. No slip condition is enforced on the pool walls.

4. Results of the VOF fluid simulations

Prior to running simulation, a water region is patched between vertical points 0 m and 0.3 m and an air region between 0.3 m and 0.35 m. We start the simulation and let it progress for a few bubble through times. As the bubble rise velocity is of order 0.3–1 m/s, the corresponding residence time is of order 0.3–1 s, depending on the injection flow rate. After stationary conditions are reached, we take statistics of the flow for a few bubbles through times as well as video recordings to compare the CFD results with the experimental data. The validation focuses on the following parameters:

- The globule detachment frequency.
- The globule effective diameter at detachment time.
- The mean void fraction in the domain.

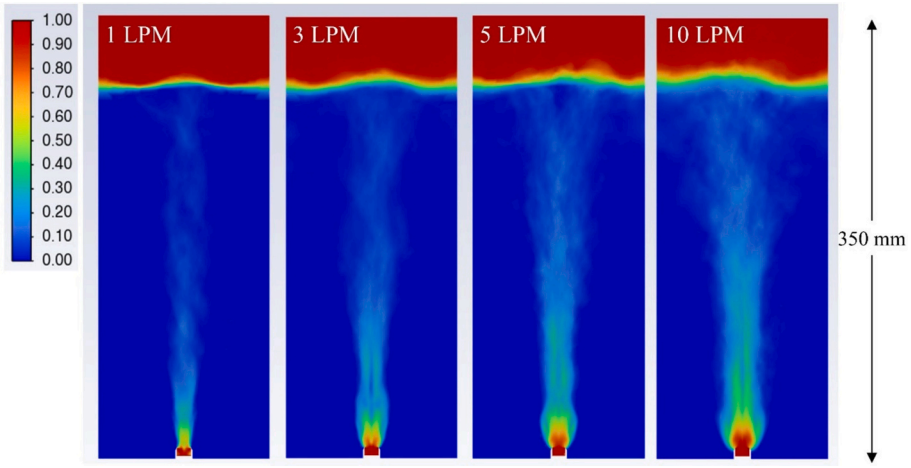

Fig. 9. Mean void fraction. From left to right: 1, 3, 5, 10 LPM.

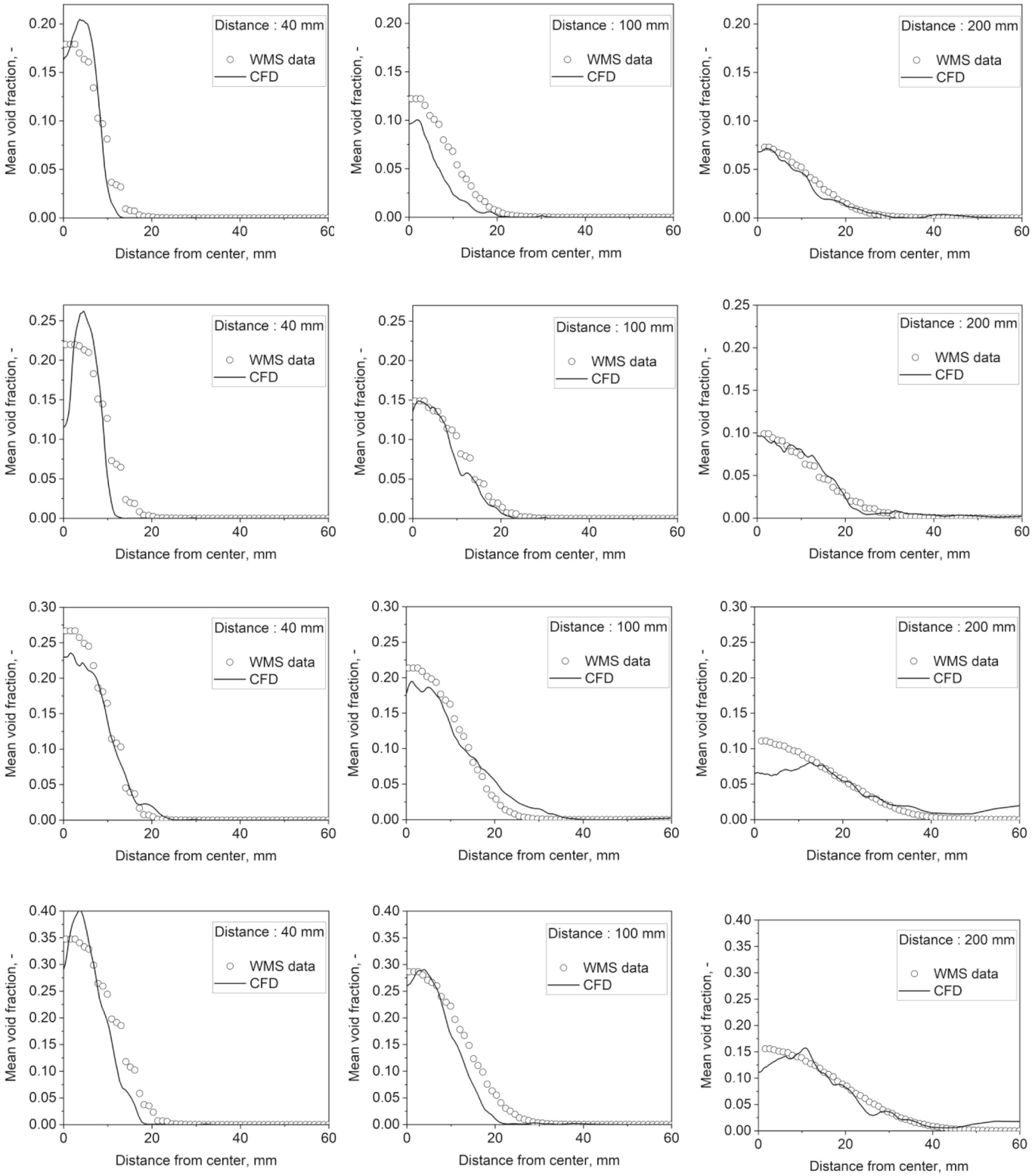

Figure 10: Mean lateral void fraction at three elevations.
From top to bottom: 1 LPM, 3 LPM, 5 LPM and 10 LPM.

Fig. 10. Mean lateral void fraction at three elevations. From top to bottom: 1 LPM, 3 LPM, 5 LPM and 10 LPM.

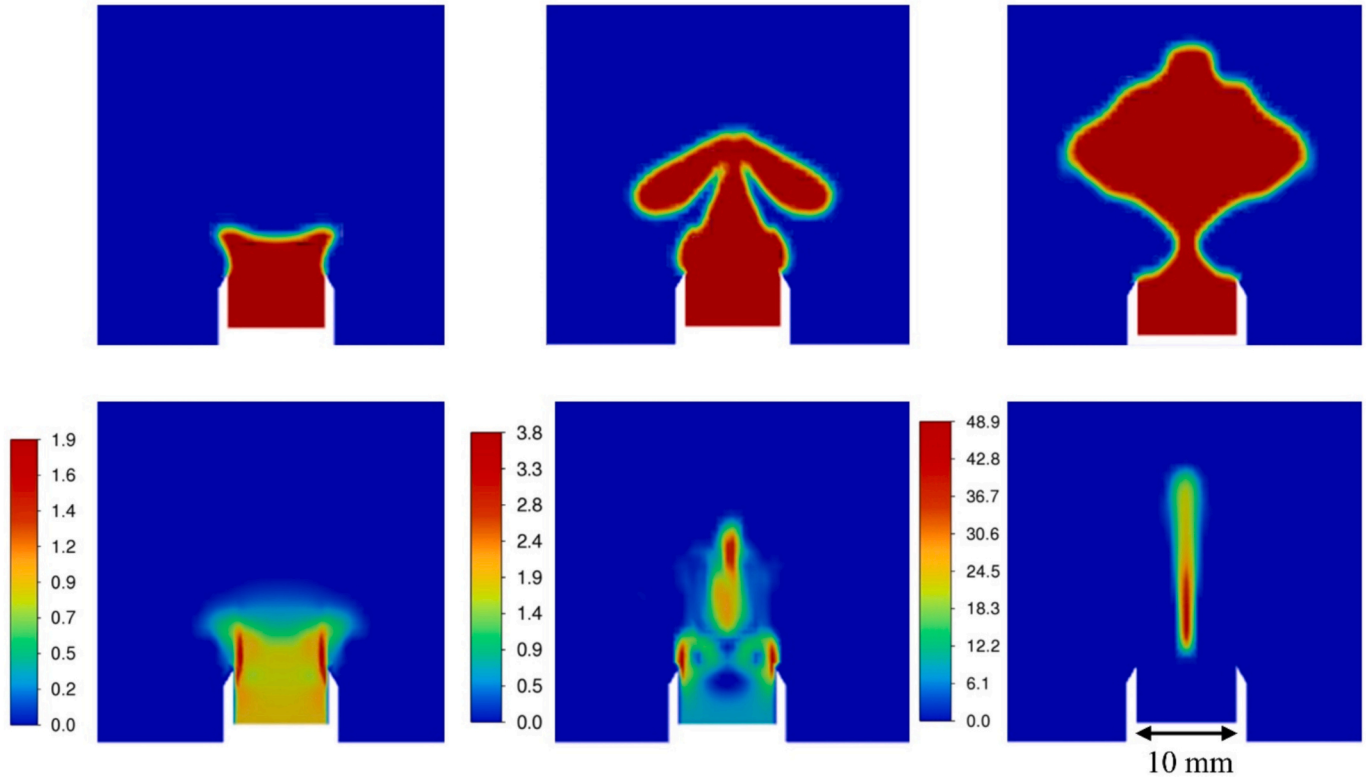

Fig. 11. Globule formation (top) and corresponding magnitude of gas velocity in m/s (bottom).

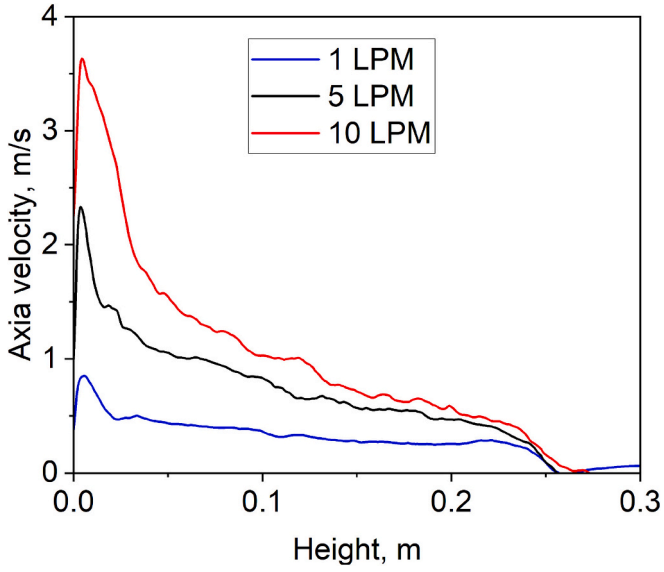

Fig. 12. Mean mixture velocity vs height.

4.1. General qualitative features of the flow

The flow appears to be aperiodic, with the globule detaching from the orifice with irregular time laps, then a complex pattern takes place along the height of the pool with frequent break-up and coalescence, in agreement with experimental observations with the HSC. Qualitatively, a sample realization of the flow for various flow rates is shown in Fig. 5, along with a counter-part experimental snapshot. One should note that the HSC provides 3D information in the depth (normal to the screen) whereas the CFD picture describes the void in the 2D vertical plane. Globally, the features are similar, with smaller, distinct spheroidal bubbles at 1 LPM, and larger, more elongated structures as the flow rate increases. Break-up and coalescence gains in intensity as the flow rate increases.

4.2. Globule detachment frequency

The globule detachment frequency is estimated from the video output by tracking globule formation at the injector in the center plane. As was considered in the experiment (Ghendour et al., 2026), a globule is deemed detached from the orifice when the globule neck closes. Fig. 6 illustrates a representative detachment sequence for the 10 LPM case. The globule starts forming at time 0 immediately after the previous globule has detached (upper left-hand corner picture). The globule grows steadily, and the neck becomes thinner with time, until the globule detaches at time 0.062 s (bottom-most picture). We note the formation of a small lump of water as well for this realization. Table 1 provides comparison between the predicted and measured detachment frequency.We note a slight over-prediction for the 1 LPM case (20 versus 16), but otherwise the simulation predicts accurately the bubble departure frequency. For the conditions of the tests, the latter has only a weak dependency on flow rate.

4.3. Globule effective diameter at detachment time

The globule mean diameter at detachment time was estimated from CFD video outputs of the central vertical plane an additional plane rotated by 90°. In both cases, it was assumed that the flow is axis-symmetric in the mean sense, such that processing a sufficiently large number of globule images yields a reliable estimate of the mean detachment diameter. In the case studies, data was processed for about 30 globules.

A similar approach was used in the analysis of the tests to process the images of the HSC (Ghendour et al., 2026). Fig. 7 outlines the series of steps involved, starting with the cropping of images to isolate the

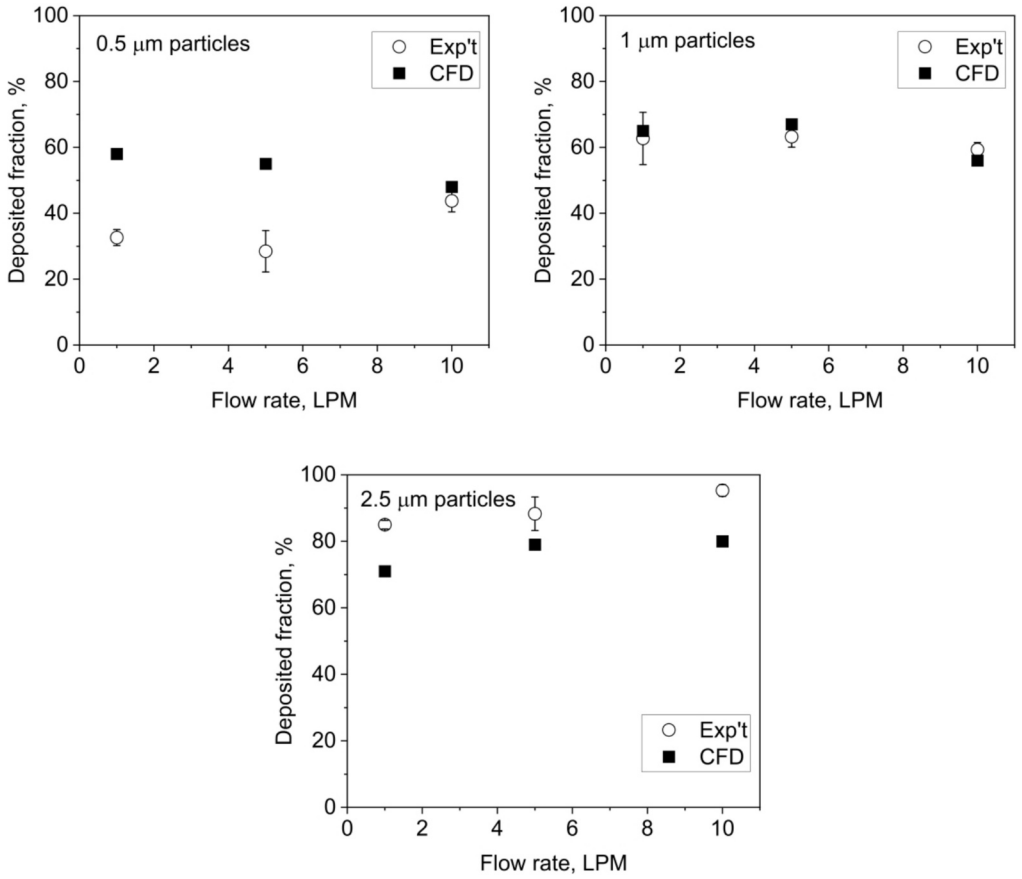

Fig. 13. Particle deposited fraction for different sizes. CFD predictions vs data.

detachment region (Process 1) and rescaling the images by considering the nozzle diameter. Subsequently, the RGB image is converted to 8-bit grayscale images and the threshold is adjusted to highlight the gas-liquid interface (Process 2). The subsequent step involves filling the holes in the bubbles, resulting in a binary image where the black and white colors represent the liquid and gas phases, respectively (Process 3). At this stage, all the bubbles in the image could be detected. However, a threshold based on the detected bubble size is applied to select only the detached globule (Process 4). Considering the axisymmetric shape of the globule at detachment, the globule diameter was estimated by calculating the equivalent diameter of the globule area from the binary image.

Results of the image processing are shown in Table 2. We display for each flow rate the experimental data, the estimated globule diameters from the 0 ^{o} and 90^{o} planes, and finally the average from the two planes. We show the standard deviation as well. As can be seen, the predicted globule diameter is in good agreement with the experimental measurement. The greatest discrepancy is 20% for the 1 LPM case. Fig. 8 summarizes the results in graphical form.

4.4. Mean void fraction

In the experiments, the instantaneous void fraction was measured with the wire mesh sensor (WMS). The WMS data was collected at three vertical locations above the tip of the nozzle, namely 40 mm, 100 mm and 200 mm. The signal was averaged over time.

In the CFD simulations, the flow field was also averaged over time for a period of 2 to 3 s, which spans about 40–60 generated globules. This gives a reasonable estimate of the mean void at a manageable CPU cost. The mean void in the central plane is shown in Fig. 9. As expected, as the flow rate increases, the void increases both in the near-field and far-field regions. We note some very slight asymmetries away from the injection zone, which indicates that the statistics there have not totally converged, but this is of no great consequence.

In Fig. 10 we show quantitative comparison between the CFD predictions and the WMS data for the mean void profiles. Globally, the predictions are in good agreement with the data, in particular in the globule formation region. Beyond this, there are some discrepancies, with the simulations predicting slightly faster diffusion near the center for the lateral void for the larger flow rates.

5. Results of particle transport simulations

5.1. Background

Particle transport computations were performed after achieving stationary hydrodynamics conditions, that is, after a few bubble through times have elapsed. After that, particles were injected at each time step, for a total duration of 0.05 s, i.e., for a typical time for a globule to form and detach from the injector. The experimental particles consisted of monodisperse spherical SiO_2 particles with density 2 g/cm^3. One thousand particles for each geometric size (0.5, 1 and 2.5 μm in diameter) were injected at every time step and distributed evenly over the inlet face.Since flow field time steps are different (the higher the gas flow rate, the smaller the time step), the total number of particles injected are 722 K, 772 K, and 1.93 M, respectively for 1 LPM, 5 LPM and 10 LPM.

5.2. Gas velocity zones and influence on particle removal modeling

It is worth noting that there are broadly two hydrodynamics zones: the near field and the far field. To illustrate this, we pick the 5 LPM case. We show in Fig. 11 respectively the void fraction and corresponding

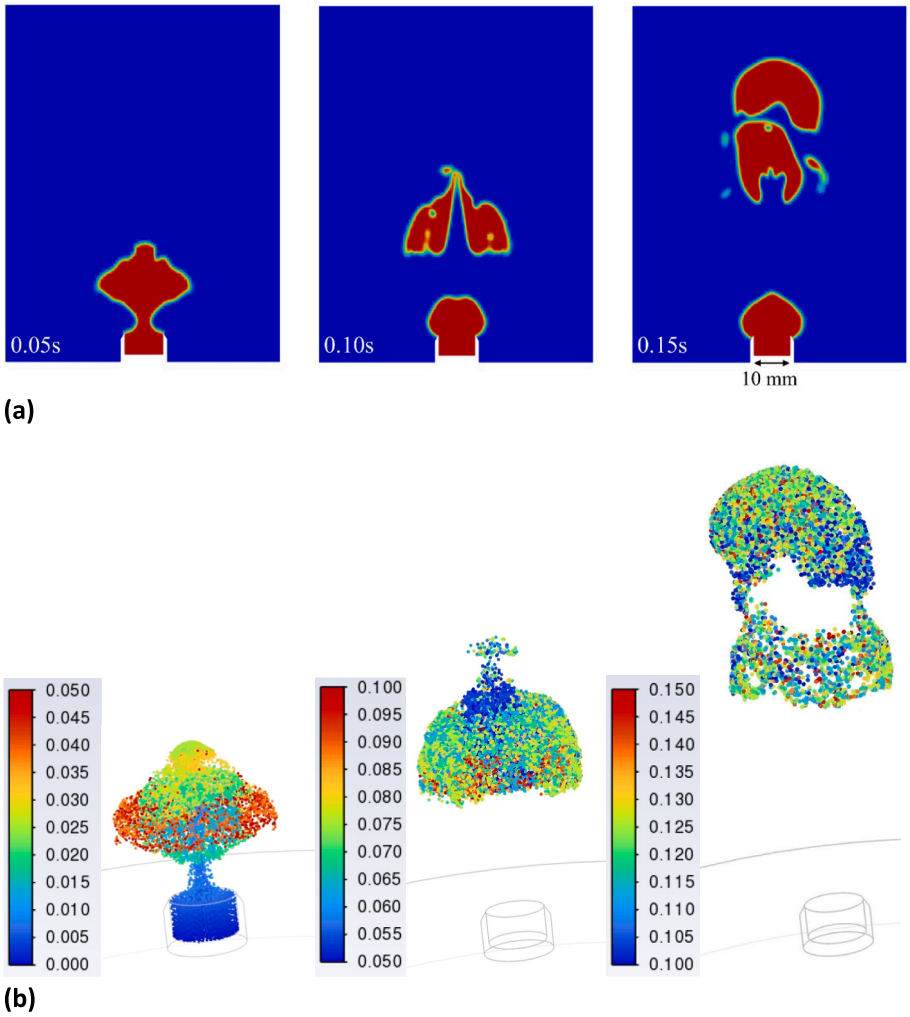

Fig. 14. (a)Globule at times 0.05 s, 0.1 s and 0.15 s (center-plane cut-view); (b)3D particle locus at times 0.05 s, 0.1 s and 0.15 s. Colored by residence time.

magnitude of velocity at three different instants spanning one globule cycle from inception to detachment. In the near field, which encompasses several injector diameters, the maximum gas velocity inside the globule before detachment gradually increases as the globule neck closes. Just before detachment, the gas velocity consists of a jet with a velocity that is orders of magnitude larger than the mean injection velocity. The latter is 1 m/s and the velocity goes up to 48 m/s just before detachment. After detachment, the high velocity inside the globule gradually decays due to fluid shearing. At some point, the mixture velocity becomes small and is more typical of a bubble rise speed (0.5–1 m/s).

These distinct velocity zones have implications for the particle transport modeling. Indeed, in the near field region, the high velocities imply that particle deposition is happening due to free flight inertial impaction on the interface. Because of this, the mesh resolution need not be too fine as the removed inertial particles typically traverse the interface cell in a single fluid time-step. On the other hand, after the mixture velocity has evened out, particle deposition is mostly through slow diffusive processes, in which case capturing particle deposition requires very high resolution and prohibitive cells counts.

Since the pool is shallow in the experiments (0.3 m), the effect of height on particle deposition is expected to be small, and hence essentially all particles which deposit do so in the near field region. Therefore, to keep the CPU reasonable, we chose to limit particle tracking in the near field region only where mesh resolution is tractable. Fig. 12 shows the mean mixture velocity as a function of height. As a result, we select the near field region to have a submergence height of 0.1 m for 1 LPM, and 0.15 m for 5 LPM and 10 LPM.

As the integration of particle equations of motion is conducted, we check at the end of each time step the location of the particle and the void fraction in the cell in which it is present. If the void fraction in the cell is zero, i.e., if the cell contains only water, then the particle is considered to have deposited and is no longer tracked. On the other hand, if a particle reaches the elevation of the free surface, it is deemed to have escaped. Careful accounting of these processes allows us to determine the overall particle removal fraction for each set of conditions.

5.3. *Comparison of particle deposition: CFD vs Data*

We compare next the experimental particle removed fraction against the CFD predictions. For the experimental results, we limit ourselves to estimates gathered from the membrane filter measurements. Results are summarized in Figs. 13 which show for each particle size the deposited fraction as a function of injection flow rate. In general, quantitative agreement between the CFD predictions and the experiments is reasonable. There is however an overestimation of deposition of the smallest particle (0.5 μm) at flow rates equal or below 5 LPM. This may be due to the absence of modeling of the lift force. The latter is known to act in the direction opposite to the wall normal direction, hence decreasing the deposition. The CFD predictions are consistent with the data with regards to the inertia-related dependency trend. Indeed, CFD

predicts that the deposition increases with particle diameter owing to inertia effects.

For a given particle size, the deposition is not very sensitive to flow rate for the range of conditions studied. This can be explained as follows: a higher flow rate produces higher velocities during globule formation, which should promote particle removal. On the other hand, the higher velocities translate into smaller surface to volume ratios for the globule, and smaller residence times in the pool, both of which phenomena lead to smaller deposition.

5.4. Particle motion inside bubbles

Fig. 14(a) shows one realization for 1 μm particle transport in the case of 5 LPM. We show the center-plane void fraction at three successive time spots and the corresponding particle plume colored by residence time (Fig. 14(b)). The original globule breaks-up within a few injector diameters, and hence airborne particles are found in two large bubbles and in much smaller ones as well. At time $t = 0.1$ s we see that particles with the least residence time (in blue) are found at the very top of the globule. These particles are projected upwards by the high velocity jet that forms around the time of globule detachment (0.05 s). This jet is responsible for breaking up the globule as seen in Fig. 14. We note as well that small droplets are generated because of the detachment process.

6. Summary and conclusions

We have simulated with CFD selected low-momentum pool hydrodynamics and particle retention tests conducted within the HECTAR project at respectively PSI and FZJ. We used the commercial code ANSYS Fluent to simulate hydrodynamics and aerosol tests for injection flow rates between 1 and 10 LPM. The VOF method was employed to model the multiphase flow, whereas the Euler-Lagrange approach was used to track the injected particles inside the bubbles. The following conclusions can be drawn from our investigations:

- The code provides reasonable estimates of the main hydrodynamics parameters, namely: the globule detachment frequency, the mean globule effective diameter at time of detachment, and the axial mean void fraction.
- The simulation generally captures the horizontal void profiles quite well, in good agreement with the WMS data. A small discrepancy is noted in the far field at 200 mm for flow rates larger or equal to 5 LPM, where the code predicts slightly larger lateral void diffusion near the central axis.
- The code predicts reasonably well the aerosol retention fraction. Analysis of the flow field inside the bubbles shed light on the very different velocity scales in the near and far field regions and helped explain why particle retention is globally insensitive to flow rate for the ranges investigated.

CRediT authorship contribution statement

A. Dehbi: Writing – original draft, Visualization, Validation, Software, Methodology, Investigation, Formal analysis, Data curation, Conceptualization. **N. Ghendour:** Formal analysis, Data curation. **B. Niceno:** Conceptualization. **D. Suckow:** Funding acquisition. **M. Klauck:** Funding acquisition.

Declaration of competing interest

The authors declare that they have no known competing financial interests or personal relationships that could have appeared to influence the work reported in this paper.

Acknowledgments

The work was performed in the framework of the research collaboration “Experimental studies and CFD simulations of aerosol removal by water pools (Pool scrubbing)” between the Paul Scherrer Institute (PSI), Switzerland and the Forschungszentrum Jülich Gmbh (FZJ) in Germany under the FZJ contract number 42276687 and the PSI quote 2021-00907.

This research collaboration is part of the HECTAR project (“Hydrodynamic Experiments to Characterize Aerosol Retention”) partly funded under contract LRT-20_11 by Swissnuclear, the association of the Swiss nuclear power station operators.

The financial support of both organizations is gratefully acknowledged.

Data availability

Data will be made available on request.

References

Abe, Y., Fujiwara, K., Saito, S., Yuasa, T., Kaneko, A., 2018. Bubble dynamics with aerosol during pool scrubbing. Nuclear Eng. Design 337, 96–107.
Albiol, T., Herranz, L., Riera, E., Dalibart, C., Lind, T., Del Corno, A., Kärkelä, T., Losch, N., Azambre, B., Mun, C., Cantrel, L., 2018. Main results of the european PASSAM project on severe accident source term mitigation. Ann. Nucl. Energy 116, 42–56.
ANSYS, Inc., 2022. ANSYS Fluent Theory Guide.
Arndt, S., Band, S., Beck, S., et al., 2019. COCOSYS 3.0 User Manual. Gesellschaft für Anlagene und Reaktorsicherheit, GRS GmbH.
Brackbill, J.U., Kothe, D.B., Zemach, C., 1992. A continuum method for modeling surface tension. J. Comput. Phys. 100, 335–354.
Dallman, R.J., Galyean, W.J., Wagner, K.C., 1990. Containment venting as an accident management strategy for BWRs with mark i containments. Nuclear Eng. Design 121, 421–429.
Dehbi, A., Cheng, X., Liao, Y., Okagaki, Y., Pellegrini, M., 2022. A comparative CFD exercise on bubble hydrodynamics using Euler-Euler and interface tracking approaches, proceedings of 19th international meeting on nuclear reactor thermal hydraulics (NURETH 19). The Square, Brussels, Belgium, March 6-11.
Fujiwara, W., Kikuchi, Y., Nakamura, T., Yuasa, S., Saito, A., Kaneko, Y., Abe, 2019. Experimental study of single-bubble behavior containing aerosol during pool scrubbing. Nucl. Eng. Des. 348, 159–168.
Gauntt, R.O., Cole, R.K., Erickson, C.M., Gido, R.I.G., Gasser, R.D., Rodriguez, S.B., Young, M.F., 2000. MELCOR Computer Code Manuals: Vol.1 & Vol.2, Rev.2, NUREG/CR-6119. U.S. Nuclear Regulatory Commission, Washington D.C., USA.
Ghendour, N., Suckow, D., Dehbi, A., Klauck, M., 2026. Experimental investigations of pool hydrodynamics and aerosol removal under low momentum injection. Nuclear Eng. Design 448, 114735.
Gupta, S., Herranz, L.E., Lebel, L.S., Sonnenkalb, M., Pellegrini, M., Marchetto, C., Maruyama, Y., Dehbi, A., Suckow, D., Kärkelä, T., 2023. Integration of pool scrubbing research to enhance source-term calculations (IPRESCA) project – overview and first results. Nuclear Eng. Design 404, 112189.
Herranz, L.E., Aguado, C., Sánchezm, F., 2020. Uncertainty quantification of in-pool fission product retention during BWR station blackout sequences. Ann. Nucl. Energy 141, 107290.
Hirt, C.W., Nichols, B.D., 1981. Volume of fluid (VOF) method for the dynamics of free boundaries. J. Comput. Phys. 39, 201–225.
Kunšek, M., Cizelj, L., Kljenak, I., 2022. New multi-fluid model of pool scrubbing in bubble rise region. Nuclear Eng. Design 395, 111873.
Laker, T.S., Ghiaasiaan, S.M., 2004. Monte-Carlo simulation of aerosol transport in rising spherical bubbles with internal circulation. J. Aerosol Sci. 35, 473–488.
Liao, Y., Li, J., Lucas, D., 2022. Investigation on pool-scrubbing hydrodynamics with VOF interface-capturing method. Nuclear Eng. Design 390, 111713.
Lind, T., Dehbi, A., Güntay, S., 2011. Aerosol retention in the flooded steam generator bundle during SGTR. Nuclear Eng. Design 241, 357–365.
Marchetto, C., Ha, K.S., Herranz, L.E., Hirose, Y., Jankowski, T., Lee, Y., Nowack, H., Pellegrini, M., Sun, X., 2022. Overview and main outcomes of the pool scrubbing lumped-parameter code benchmark on hydrodynamic aspects in IPRESCA project, proceedings of 19th international meeting on nuclear reactor thermal hydraulics (NURETH 19). The Square, Brussels, Belgium, March 6-11.
Marcos-Crespo, M., Gómez-Moreno, F., Melches-Serrano, I., Martin-Espigares, M., López Jiménez, J., 1993. LACE-España Experimental Programme on the Retention of Aerosols in Submerged Beds. CIEMAT ITN/TS-08/DP-93.
Motegi, K., Sibamoto, Y., Kukita, Y., 2022. Nonuniform particle distribution and interference between removal mechanisms during unsteady aerosol deposition from a rising spherical bubble. J. Nucl. Sci. Technol. 59 (8), 1037–1046.
Nakamura, Y., Fujiwara, Y.K., Kikuchi, W., Yuasa, T., Kaneko, A., Abe, Y., 2019. Experimental study on decontamination effect of gas-liquid two-phase flow behavior with condensation during pool scrubbing. In: The 27th International Conference on Nuclear Engineering (ICONE27).

Owczarski, P.C., Burk, K.W., 1991. A Code for Calculating Fission Product Capture in Suppression Pools, Technical Report NUREG/CR-5765 TI92 003256.
Paul, D.D., Flanigan, L.L., Cudnik, R.A., Cunnane, J.C., Coller, R.P., 1985. Radionuclide Scrubbing in Water Pools Volume 1: Gas-Liquid Hydrodynamics, NP-4154. Electric Power Research Institute, Palo Alto, CA.
Paul, D.D., Flanigan, L.L., Cudnik, R.A., Cunnane, J.C., Coller, R.P., 1991. Radionuclide scrubbing in water pools Volume 2: Gas-Liquid Hydrodynamics with Full Scale Downcomer and Horizontal Vent, NP-4154-L. Electric Power Research Institute, Palo Alto.
Ramsdale, S.A., Güntay, S., Friederichs, H.G., 1995. BUSCA-JUN91 Reference Manual. Technical Report, Report number PSI-95-05. Paul Scherrer Institut, Switzerland.
Sun, D., 2021. Numerical study on particle decontamination from spherical bubbles in scrubbing pools by using Eulerian–Lagrangian method. Powder Technol. 393, 692–704.
Sun, D., 2022. Particle decontamination from elliptical bubbles in scrubbing pools simulated using Eulerian–Lagrangian method. Powder Technol. 397, 117003.
Sussman, M., 1994. A level set approach for computing solutions to incompressible two phase flow. J. Comput. Phys. 114, 146–159.
Wassel, A.T., Mills, A.F., Bugby, D.C., Oehlberg, R.N., 1985. Analysis of radionuclide retention in water pools. Nuclear Eng. Design 90, 87–104.
Zhu, M., Dehbi, A., Sato, Y., Niceno, B., 2019. Simulations of particle transport inside bubbles using coupled interface and Lagrangian tracking approaches. In: 18th International Topical Meeting on Nuclear Reactor Thermal Hydraulics (NURETH-18), pp. 3677–3688 (Portland, USA).